metals

MDPI

Article

Effect of Oxygen on Growth Mechanism of SiO_2 Inclusions in Non-Agitated Melts

Suwam Kumar [1], Angshuman Podder [1], Muhammad Nabeel [1], André B. Phillion [1] and Neslihan Dogan [2,*]

[1] Department of Materials Science and Engineering, McMaster University, Hamilton, ON L8S 4L8, Canada; kumars66@mcmaster.ca (S.K.); angshuman.podder.leo@gmail.com (A.P.); nabeelm@mcmaster.ca (M.N.); philliab@mcmaster.ca (A.B.P.)

[2] Department of Materials Science and Engineering, Delft University of Technology, 2628 Delft, The Netherlands

* Correspondence: n.d.dogan@tudelft.nl

Abstract

This study investigates the growth and evolution of SiO_2-based inclusions in Si-killed steel under stagnant conditions and varying oxygen levels. Deoxidation experiments were conducted in a high-temperature furnace using commercial FeSi, with systematic variations in holding time and total oxygen content. Automated SEM–EDS analysis was employed to quantify inclusion size, number density, and chemical composition. Under stagnant conditions, SiO_2 inclusions were observed to grow and coarsen in the absence of melt agitation, following a $t^{1/3}$ scaling law. In high-oxygen melts, rapid inclusion growth was dominated by Stokes collision mechanisms, resulting in the formation of inclusions in the size range of 1–5 µm, which were subsequently removed by flotation. In contrast, low-oxygen melts exhibited slower growth kinetics governed primarily by Brownian motion and Ostwald ripening, producing smaller inclusions with characteristic sizes of 1–2 µm. These results demonstrate that the initial oxygen content plays a decisive role in controlling the dominant growth mechanisms and the extent of inclusion coarsening in non-agitated steel.

Keywords: Brownian motion; Stokes collisions; deoxidation; SiO_2 inclusions; number density

1. Introduction

In Si-killed steels, silicon acts as the primary deoxidant, leading predominantly to the formation of silica and different silicate inclusions [1–4]. These inclusions may adhere to refractory surfaces and contribute to flow disturbances and clogging during continuous casting operations [5–7]. Consequently, understanding the formation, growth, and removal behavior of non-metallic inclusions in Si-killed steels is essential for improving steel quality and overall performance.

Most previous studies on inclusion evolution have focused on Al-deoxidized and/or Ca-treated steels, where inclusion chemistry and morphology are governed by complex multi-component interactions [8–10]. These investigations have provided significant insight into inclusion growth and coarsening mechanisms, particularly under turbulent or gas-stirred conditions. However, such systems often obscure the fundamental growth behavior due to the simultaneous effects of multiple deoxidants, interfacial reactions, and hydrodynamic forces [11]. In contrast, Si deoxidation offers a comparatively simpler system in which inclusion evolution can be examined with reduced chemical complexity [11]. This is also relevant for specific steel grades where aluminum is restricted, such as tire cord steels,

Academic Editor: Joan-Josep Suñol

Received: 24 April 2026
Revised: 26 May 2026
Accepted: 28 May 2026
Published: 4 June 2026

spring steels, and certain electrical steels, in which hard Al_2O_3 inclusions are undesirable due to their detrimental effect on formability and fatigue performance [1,12,13].

Inclusion growth in liquid steel has been widely described in terms of diffusion-controlled and collision-driven mechanisms. Classical Lifshitz–Slyozov–Wagner (LSW) theory describes diffusion-controlled coarsening (Ostwald ripening) in dilute systems [14–17], whereas collision-induced growth has been modeled using population balance approaches based on Brownian motion, turbulent shear, and differential settling (Stokes collisions) [18–20]. Experimental studies have shown that Ostwald ripening is typically dominant for small inclusions at low volume fractions, while collision-driven mechanisms become more significant with increasing particle size and number density [14,15]. However, most of these studies have been conducted in Al-deoxidized or multi-component systems, and their direct applicability to Si-killed steel, particularly SiO_2 inclusions, remains limited. This limitation can be addressed through controlled laboratory experiments using Si-only or Fe–Si deoxidation systems, combined with automated SEM–EDS characterization and population balance modeling.

Recent investigations have begun to address inclusion evolution in Si-killed or Al-restricted systems. Studies on Si–Mn-killed steels during ladle refining have reported compositional and morphological evolution of inclusions under varying processing conditions [21], while research on aluminum-free steelmaking has highlighted the interaction between silica-based inclusions and slag phases [11]. Other recent works have emphasized the importance of particle size distribution and number density in governing inclusion coarsening and removal behavior [22–24]. These studies indicate that inclusion evolution is governed by a coupled interaction between thermodynamics, interfacial kinetics, and transport processes.

Among the governing parameters, including thermodynamic driving forces, interfacial kinetics, transport processes, and melt flow conditions, the oxygen content of the steel plays a key role in determining inclusion evolution, as it directly influences oxide formation [8,25], interfacial reaction kinetics [26], and mass transport processes [27,28]. Variations in oxygen content affect nucleation density and supersaturation, which in turn influence particle size distribution and subsequent growth behavior. Although the influence of oxygen content of the steel on inclusion chemistry is well established, its role in governing the transition between different physical growth mechanisms, particularly in Si-killed steels under stagnant conditions, has not been systematically examined.

In addition, many experimental studies have been performed under conditions where fluid flow and turbulence significantly affect inclusion motion and collision frequency [29,30]. While such conditions are representative of industrial processes, they complicate the identification of fundamental growth mechanisms. Investigating inclusion evolution under non-agitated or stagnant conditions allows the influence of diffusion and gravity-driven interactions to be isolated, providing clearer insight into the intrinsic growth behavior of inclusions.

In this study, the evolution of SiO_2 inclusions in a Fe–Si–O system is investigated under controlled stagnant conditions at 1873 K, allowing fundamental growth kinetics to be examined with minimal influence from flow-induced collision mechanisms. The initial oxygen content of the melt is systematically varied to evaluate its influence on inclusion size, number density, and volume fraction over time, with particular emphasis on inclusions in the 1–5 μm size range. A series of controlled high-temperature experiments is conducted to monitor inclusion evolution and corresponding changes in steel composition. Experimental observations are combined with analytical modeling to assess the relative contributions of diffusion-controlled and collision-driven growth mechanisms, as well as inclusion removal by flotation. The objective is to establish a quantitative relationship between oxygen content,

particle size distribution, and the dominant mechanisms governing inclusion evolution in Si-killed steels.

1.1. Growth/Coarsening Theories

1.1.1. Diffusion Controlled Growth

Diffusion-controlled growth is a process where transport of solute atoms takes place from a surrounding matrix (liquid/solid) towards the secondary phase/matrix interface. This mechanism becomes important when the concentration gradient of the solute is large enough to support growth. In inclusion studies [14–16,31], oxygen diffusion is considered one of the primary factors driving inclusion growth. Consequently, the growth rate is determined by the rate at which solute atoms diffuse from the molten steel to the inclusions. This can be expressed as [27,32,33]

$$\frac{\Delta r}{\Delta t} = D_O \frac{(C_O - C_{eq})}{(C_P - C_{eq})} \tag{1}$$

where $\Delta r/\Delta t$ is the particle growth rate, r is the particle radius (m) at time t (s), D_O is the diffusion coefficient of oxygen, C_O is the dissolved oxygen concentration in liquid steel (kg/m^3), C_{eq} is the equilibrium oxygen concentration in the particle in contact with the steel (kg/m^3), and C_P is the stoichiometric oxygen concentration of a silica particle (kg/m^3).

The characteristic time, t_{90}, required for the particle volume to reach 90% of its equilibrium value can be expressed following the formulation of Wert and Zener [34], as given by Equation (2):

$$t_{90} = \frac{1}{D_O} \cdot \frac{(C_P - C_{eq})}{(C_i - C_{eq})} \cdot \bar{r}_f^2 \tag{2}$$

Here, C_i denotes the dissolved oxygen concentration in liquid steel prior to deoxidant addition (kg/m^3), and $\bar{r}_f$ represents the mean particle radius after diffusion-controlled growth (m).

1.1.2. Coarsening Driven by Ostwald Ripening

Ostwald ripening is a diffusion-controlled growth process in which larger particles grow at the expense of smaller ones [35–39]. This phenomenon occurs because smaller particles, having higher curvature, possess higher chemical potential, which causes them to dissolve and their dissolved species to diffuse toward and deposit onto larger particles. This process is thermodynamically driven as the system naturally moves towards a more stable state by minimizing the total surface area. In metallurgical systems, this process is further governed by the Gibbs–Thomson effect, where the higher curvature of smaller particles increases their equilibrium solubility in the surrounding matrix. This curvature dependence is expressed by

$$C(r) = C_\infty \exp\left(\frac{2\gamma V_m}{rRT}\right) \tag{3}$$

where $C(r)$ (mol/m^3) is the equilibrium solubility around a particle of radius r (m), C_∞ (mol/m^3) is the solubility at a flat interface, γ (J/m^2) is the interfacial energy, V_m (m^3/mol) is the molar volume of the solid inclusion phase, R (J/mol/K) is the universal gas constant, and T (K) is the absolute temperature.

Consequently, dissolved species diffuse from regions around smaller particles toward larger ones, creating a net flux that promotes growth of the latter. Such diffusion-controlled coarsening becomes increasingly significant at longer holding times or at lower volume fractions of the dispersed phase, where collision-driven coalescence is less frequent and solute redistribution dominates the overall growth behaviour [37,39].

1.1.3. Collision Growth by Brownian Motion

Brownian motion describes the random motion of very small particles suspended in a liquid due to collisions with surrounding atoms or molecules. According to the Einstein–Stokes theory, the diffusivity D of a spherical particle in a liquid is given by [40]

$$D = \frac{k_B T}{3\pi\mu d} \tag{4}$$

where k_B is the Boltzmann constant (1.3806×10^{-23} J/K), T is the absolute temperature (K), μ is the dynamic viscosity of the liquid (Pa·s), estimated from Brooks et al. [41] as Equation (5), and d is the particle diameter (m). The diffusivity increases with temperature and decreases with both viscosity and particle size, indicating that smaller particles experience stronger Brownian motion.

While smaller particles exhibit higher Brownian diffusivity, Smoluchowski's collision theory [42] demonstrates that for a monodisperse population (particles of equal size), the collision frequency becomes independent of particle size as the enhanced diffusivity is offset by the reduced geometric collision cross-section. Consequently, Brownian collisions are primarily important during the early stages of deoxidation when inclusions are in the nanometer to sub-micrometer size range, becoming less significant as particles grow and mechanisms such as turbulent and Stokes collisions begin to dominate. The viscosity of steel is taken as a function of temperature as follows:

$$\mu = 19.627 - 0.0091 \cdot (T - 273) \quad \text{(mPa·s)} \tag{5}$$

The evolution in volumetric particle number density, $N_V(t)$ is given by [14,20,42]

$$N_V(t) = \frac{N_{V,0}}{1 + \frac{8k_B T N_{V,0}}{3\mu} t} \tag{6}$$

where $N_{V,0}$ is the initial volumetric particle number density.

1.1.4. Growth Induced by Differences in Ascending Velocity

The ascent velocity of a particle in a fluid is governed by Stokes' law, which states that larger inclusions rise faster than smaller ones due to buoyancy arising from density differences [18]. This velocity difference induces relative motion between particles, leading to collisions and potential coalescence known as Stokes collisions. According to Miyashita et al. [9], the resulting growth of inclusions due to these interactions is expressed by [15]

$$r(t) = r_0 \left[1 - \frac{g f_V (\rho_{steel} - \rho_P) r_0 t}{18\mu} \right]^{-1} \tag{7}$$

where g is the gravitational acceleration (9.8 m/s^2), f_V represents the volume fraction of inclusion particles, and ρ_{steel} and ρ_P are the densities of liquid steel and inclusion particles, respectively (kg/m^3).

1.1.5. Growth Induced by Laminar Shear Collisions

In quiescent or mildly convective melts, inclusions can collide due to velocity gradients within laminar flow fields. When adjacent fluid layers move at different velocities, inclusions entrained in the flow experience differential motion, resulting in collisions and coalescence. This mechanism, known as laminar shear collision, is particularly effective when the shear rate (du/dx) is moderate and the inclusion concentration is sufficiently high.

2. Methodology

2.1. Experiments

A series of high-temperature deoxidation experiments were conducted in a resistance-heated vertical tube furnace, following a procedure detailed in the study by Podder et al. [43], with key aspects summarized here. First, 295 g of Fe-O melt was prepared from electrolytic iron and Fe_2O_3 in a MgO crucible. The crucible was then placed in the furnace and heated to 1600 °C under an argon atmosphere. To minimize oxygen contamination, high-purity (99.999%) argon gas was passed through titanium turnings at 700 °C at a flow rate of 0.5 L/min prior to entering the furnace, maintaining the oxygen partial pressure below $\sim 10^{-12}$ atm. After holding at 1600 °C for 30 min, a pin sample (5 mm diameter, 6–7 cm length) was extracted to determine the initial total oxygen (T.O.) content of the melt. Subsequently, Fe80Si (1.2 wt.%Al) was added through a feeding tube to initiate deoxidation. Commercial-grade Fe80Si was deliberately selected over pure Si metal to more accurately simulate industrial conditions and trace aluminum interactions relevant to Al-restricted steel grades, as outlined in Section 1. Melt samples were then collected at specified time intervals using a quartz tube to monitor inclusion evolution, and were rapidly quenched in water to suppress secondary inclusion formation.

For the current study, three deoxidation experiments were considered and they were conducted with Fe80Si with varying initial oxygen contents (550, 321, and 136 ppm). In these experiments (designated as E550, E321, and E136), varying amounts of Fe_2O_3 (1.01 g for E550, 0.25 g for E321, and 0 g for E136) were used to investigate the effect of oxygen on inclusion evolution and growth behavior. For E550, pin samples were taken at 30, 60, 300, and 600 s, while for E321 and E136, pin samples were taken at 30, 300, and 600 s. A summary of the average chemical composition for each experiment after FeSi addition is given in Table 1, with the measured T.O. at each time interval given in Table 2.

Table 1. Average chemical composition of the lab-produced steel samples after FeSi addition.

Exp.	C (wt.%)	Mn (wt.%)	Si (wt.%)	Al (ppm)	S (ppm)
E550	0.008	0.039	0.121	40	23
E321	0.008	0.045	0.14	40	16
E136	0.014	0.043	0.155	50	17

Table 2. Evolution of T.O. content of lab-produced steel samples with time after FeSi addition.

Time (s)	T.O. (ppm)		
	E550	E321	E136
0	550	321	136
30	527	250	120
60	507	-	-
300	250	190	90
600	156	182	87

2.2. Inclusion Characterization

Each pin sample was cross-sectioned vertically for inclusion analysis. The exposed cross-sections were first ground using silicon carbide (SiC) paper with grit ranging from 120 to 1200, followed by sequential polishing with water-free diamond suspensions of 6, 3, and 1 μm average particle sizes. An automated scanning electron microscope (SEM, JEOL 6610LV, JEOL Ltd., Tokyo, Japan) equipped with energy-dispersive spectroscopy (EDS) and feature analysis software (AZtec v6.0) was used to identify and analyze inclusions

on the polished sections. The AZtec software detected inclusions based on their contrast with the steel matrix and determined each inclusion's equivalent circular diameter (ECD), circularity, and chemical composition, while providing the projected area of each individual inclusion from which the overall 2D (area) number density was subsequently calculated.

The SEM-EDS examination was conducted at 800× magnification with an accelerating voltage of 15 kV, an emission current of 51.4 µA, and a spot size of 62 pct. For each sample, an 8 mm^2 field of view (FOV) was analyzed. Smaller inclusions (<1 µm in diameter) were excluded because they are difficult to analyze at larger FOV (and hence lower resolution).

2.3. Calculation Methods

The equivalent circular diameter or 2D particle diameter ($d_{A,i} = 2r_{A,i}$), represents the diameter of a circle with an area equal to the area of the detected feature. For each inclusion, this was calculated as follows:

$$d_{A,i} = 2 \times \phi \sqrt{\frac{\mathrm{A}_i}{\pi}} \tag{8}$$

where A_i represents the feature area which is the number of pixels within an inclusion as identified by the AZtec software, and ϕ is the pixel size in µm.

The 3D volume fraction (f_V) can be estimated from the 2D measurements, following a relationship developed by Fullman [44] for spherical particles. This relationship begins by determining the arithmetic mean of the 3D particle radius $\bar{r}_V$, as follows:

$$\bar{r}_V = \frac{\pi}{2} \cdot \bar{r}_{A(\mathrm{har.})} = \frac{\pi}{2} \cdot \frac{n}{\sum_{i=1}^{n} (1/r_{A,i})} \tag{9}$$

where $\bar{r}_{A(\mathrm{har.})}$ denotes the harmonic mean of the measured 2D particle radii, $r_{A,i}$ represents the 2D radius of an individual particle i, and n represents the total number of measured particles. The relationship between the 3D number density N_V (#/mm^3) and the measured 2D number density, N_A (#/mm^2) is then given by

$$N_V = N_A / 2\bar{r}_V \tag{10}$$

Finally, f_V of inclusions is determined as

$$f_V = (4/3)\pi \bar{r}_V^3 N_V \tag{11}$$

Inclusion data obtained via the Automated Feature Analysis (AFA) technique are limited by their 2D nature, presenting inherent challenges in stereological analysis. To address these limitations, researchers commonly employ the population density function (PDF) approach for analyzing inclusion size distributions, as it significantly reduces user-induced biases and ensures a more objective interpretation of the data [45–49]. The PDF, expressed in units of length^{-4}, is defined by the following equation:

$$\mathrm{PDF} = \frac{n_v(L_{XY})}{L_Y - L_X} \tag{12}$$

where $n_v(L_{XY})$ denotes the frequency of inclusions per unit volume within a specified size bin, and $L_Y - L_X$ represents the bin width.

In this study, the Crystal Size Distribution (CSD) correction software (version 1.61) was also utilized to convert the 2D AFA data into a three-dimensional (3D) inclusion size distribution. The software accepts the raw inclusion measurements, specifically, area, length, and width as input parameters and assumes spherical inclusion geometry for

calculation purposes. Based on these inputs, the program computes the corrected PDF size distribution.

3. Results

3.1. Characterization of Inclusions in Si-Killed Steel

Figure 1 shows SEM-EDS analysis of inclusions from one of the experimental samples (E550), obtained 30 s after Fe80Si (1.2 wt.%Al) deoxidation. It was found that silica (SiO_2) was the dominant form of inclusions, representing at least 80% of the total analyzed inclusions, while the remaining inclusions consisted of varying levels of alumina ranging from 1 to 15% mostly in E136. The inclusions were found to be circular in nature as can be seen in Figure 1. Although the presence of Al in the FeSi alloy suggests the possible formation of Al–Si–O complex inclusions, the number of such inclusions identified in the analyzed area was limited and did not provide a statistically representative dataset for meaningful quantitative analysis. Therefore, for the purpose of this study, only silica inclusions were analyzed.

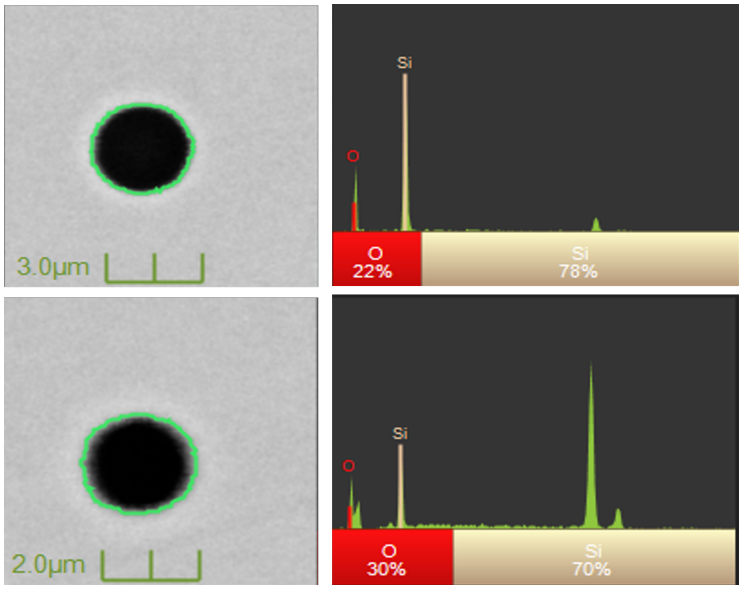

Figure 1. SEM–EDS analysis of inclusions from sample E550 showing that silica (SiO_2) is the dominant inclusion type with circular morphology.

3.2. Mean Inclusion Size and Inclusion Volume Fraction

Figure 2 illustrates the average ECD of the silica inclusions with time. As can be seen, there is an overall increase in the ECD values for all three experiments with higher oxygen leading to larger particle sizes: $\bar{d}_{A,i}$(E550) > $\bar{d}_{A,i}$(E321) > $\bar{d}_{A,i}$(E136). Additionally, mean particle growth rates, $\Delta(\bar{d_A})/\Delta t$, were determined between successive sampling times. For E550, the rates show an initial increase in particle size, followed by a decrease after 300 s, with 7.13 nm/s (30–60 s), 0.41 nm/s (60–300 s), and –0.59 nm/s (300–600 s). In E321, we observed a slower but consistently positive growth throughout 600 s, with 0.51 nm/s (30–300 s) and 0.74 nm/s (300–600 s). For E136, growth remained limited at 0.14 nm/s (30–300 s) and 0.28 nm/s (300–600 s). It is important to point out that the mean inclusion size decreases systematically with oxygen content (E550 > E321 > E136), emphasizing the role of initial oxygen content in determining both the extent of oxide formation and the dominant growth pathway. This will be discussed in Section 4.5.

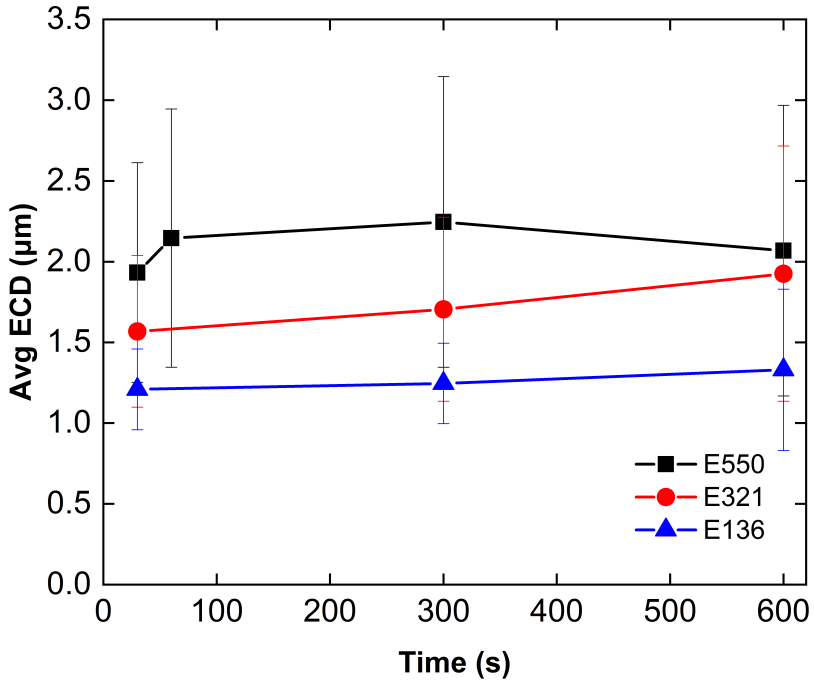

Figure 2. Evolution of average ECD for silica inclusion with time at 1873 K for E550, E321 and E136.

The changes in inclusion volume fraction, f_V were calculated using Equations (9)–(11) for various holding times. For each experiment, the overall rate of decrease in f_V was determined as the average slope over the entire holding period from 30 to 600 s. Figure 3 illustrates the evolution in f_V over time for all three experiments, from which it can be seen that the rate of volume fraction decreases in the following order:

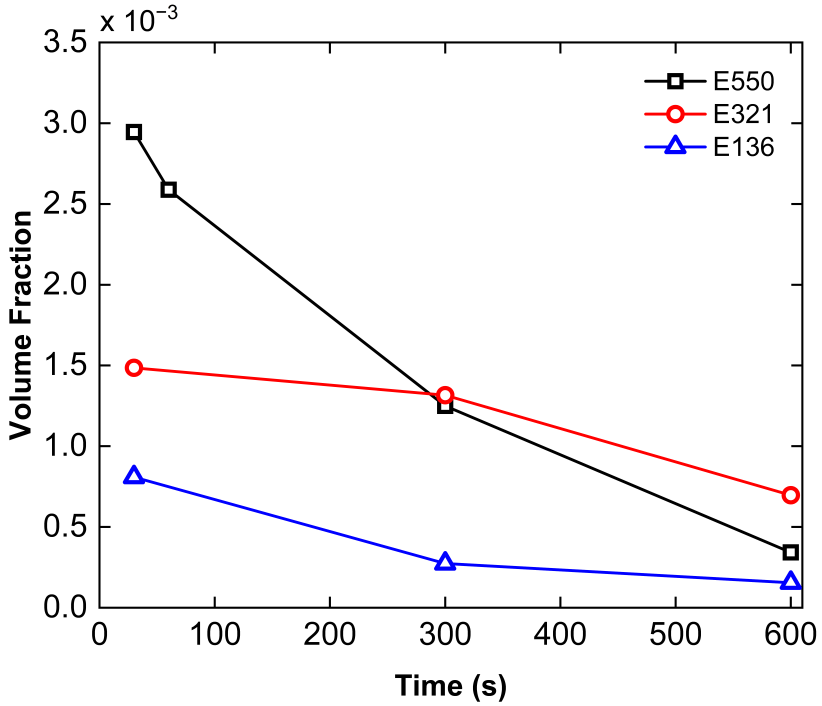

Figure 3. Evolution in f_V for all three experiments as calculated using the experimentally measured N_A and Equation (11).

E550 (4.6×10^{-6} s^{-1}) > E321 (1.4×10^{-6} s^{-1}) > E136 (1.2×10^{-6} s^{-1}). This trend aligns with the observed reduction in total oxygen content, which is closely linked to the removal

of non-metallic inclusions. The rapid decrease in dissolved oxygen following deoxidizer addition promotes inclusion formation, enabling their subsequent separation from the melt [50,51], likely through flotation and/or adherence to the crucible walls. Moreover, in E550, volume fraction decreased rapidly compared to E321 and E136 owing to higher oxygen content, leading to higher collision rates and higher removal rates, both of which contributes to a decreasing inclusion mass fraction in the melt. The interplay between growth factors and removal factors results in a characteristic feature in the dynamics, as will be shown later.

3.3. Particle Size Analysis

Figure 4 illustrates how the silica particle size fractions evolve over time at 1873 K for E550, E321, and E136 samples by categorizing particles into four uniform distinct size ranges. It is generally observed that smaller silica particles decrease in proportion, while larger particles become more prevalent. Specifically, for E550 samples, the percentage of smaller inclusions (1–2 μm) drops from 60% at $t = 30$ s to 40% at $t = 600$ s, whereas larger inclusions (3–5 μm) notably increase, with the 4–5 μm range climbing from 2% to 15%. Likewise, for E321 samples, inclusions measuring 1–2 μm diminish from 80% to 60% within the same time frame, while 3–4 μm inclusions rise from 1% to 10%, and those in the 4–5 μm category grow slightly to 5%. In contrast, E136 samples demonstrate a modest shift, with 1–2 μm inclusions continuing to be prevalent, slightly reducing from 93% at $t = 30$ s to 85% at $t = 600$ s, while larger inclusions show only slight increments.

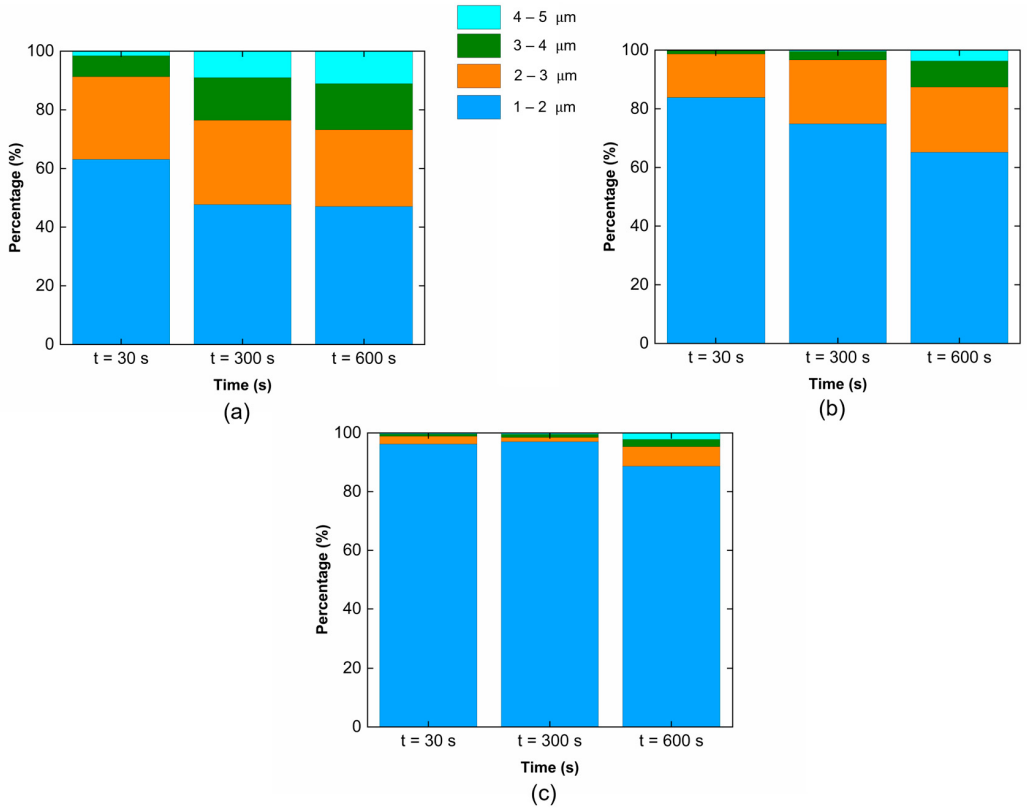

Figure 4. Variation in size distribution of the silica inclusions as a function of holding time at 1873 K: (**a**) E550 samples, (**b**) E321 samples and (**c**) E136 samples.

4. Discussion

4.1. Growth Kinetics

Throughout this section, two distinct inclusion evolution mechanisms are considered: growth and coarsening. Growth is a non-competitive process in which inclusions increase

in size through diffusion-controlled mass transfer and/or collision-driven agglomeration, leading to an increase in total inclusion mass. In contrast, coarsening (Ostwald ripening) is a competitive, near-equilibrium process governed by the Gibbs–Thomson effect, where larger inclusions grow at the expense of smaller ones, resulting in constant total inclusion mass and a decreasing particle number. Below, we first examine diffusion-controlled growth to assess whether it can account for the experimentally observed inclusion growth kinetics.

The deoxidation process of liquid steel initially containing 550 ppm oxygen deoxidized with FeSi was analyzed using the diffusion-based model described by Equation (2). The relationship between $\bar{r}_f$ and t_{90} was obtained by substituting $C_i = 3.85$ kg/m^3, $C_P = 1.41 \times 10^3$ kg/m^3, and $D_O = 2.91 \times 10^{-9}$ m^2/s [52] into Equation (2). The equilibrium dissolved oxygen concentration, C_{eq}, was calculated for each experimental condition using FactSage (v8.1) based on the input dissolved oxygen values listed in Table 2. The results, shown in Figure 5, indicate that t_{90} is approximately 0.0015 s at $\bar{r}_f = 0.8$ μm and 1 s at $\bar{r}_f = 2.6$ μm. These calculations suggest that particle growth by diffusion under the investigated conditions proceeds extremely rapidly, implying that the observed growth of deoxidation products during the holding period of 30–600 s at 1873 K cannot be attributed solely to diffusion-controlled growth. Identical behavior was observed for the E321 and E136 melts, confirming that pure diffusional growth is not rate-controlling for any of the three oxygen levels investigated.

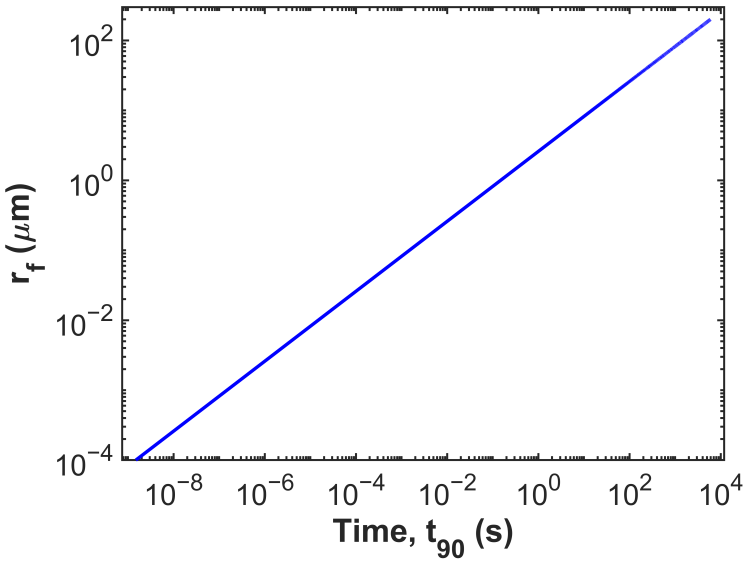

Figure 5. Relationship between particle radius and t_{90} calculated from Equation (2) for particle growth by diffusion.

Previous studies [15,16,31,53] on precipitation reactions employ Ostwald ripening to explain the coarsening of particles in fluids. According to the classical Lifshitz–Slyozov–Wagner (LSW) theory [35,36], coarsening in dilute dispersions is governed by diffusion-controlled mass transfer, driven by the Gibbs–Thomson effect. The LSW theory is based on several key assumptions: infinitely dilute dispersions with negligible volume fraction of the precipitate phase ($\phi \to 0$), spherical particles, and quasi-steady-state diffusion around each particle. Under these assumptions, LSW theory predicts that the cube of the mean particle radius increases linearly with time, yielding a characteristic $\bar{r}^3 \propto t$ growth law, with the number density of particles decreasing as $N_v \propto t^{-1}$ and the supersaturation decaying as $\Delta C \propto t^{-1/3}$. Accordingly, particle growth via Ostwald ripening based on the classical LSW (Lifshitz, Slyozov [35] and Wagner [36]) can be expressed as

$$\bar{r}^3 - \bar{r}_0^3 = \alpha_{\mathrm{LSW}}\, k_d\, t \tag{13}$$

where $\bar{r}$ is the mean particle radius (m) at time t, $\bar{r_0}$ is the mean particle radius at the onset of Ostwald growth (m), α_{LSW} is the coarsening coefficient (=4/9) and k_d (m^3/s) is the rate constant for the diffusion-controlled growth process and given by

$$k_d = \frac{2\gamma_{PL} D_O V_O C_O}{RT(C_P - C_O)} \tag{14}$$

where R is the gas constant (J/mol/K). The molar volume of oxide per oxygen mole, V_O (m^3/mol), is given by $V_O = M_O/C_P$, where M_O is the atomic weight of oxygen and C_P is the oxygen concentration in oxide (silica) particle (kg/m^3). The interfacial energy γ_{PL} (J/m^2) between the oxide and molten steel was calculated as described in Appendix A. The effective rate constant for Ostwald ripening can then be written as $K = \alpha_{\mathrm{LSW}}\, k_d$, which quantifies the rate of particle growth under diffusion-controlled conditions.

The evolution of inclusion radius can be described by the following generalized growth equation employed in the study of particle suspensions [54]:

$$\bar{r}^n(t) - \bar{r}_0^n = K\, t, \tag{15}$$

where K is an effective rate constant. Here, by setting n = 3, it is interesting to see that the mathematical form is similar to the classical Lifshitz–Slyozov–Wagner (LSW) theory of diffusion-controlled Ostwald ripening (See Equation (13)) [35,36]. Population balance treatments of collision and coagulation also predict the same cubic growth law (Equation (15)). In this context, however, the effective rate constant K reflects collision frequency and coalescence efficiency rather than diffusion and is determined by fitting to experimental data [54]. For example, Ratke [54] showed that coarsening in liquid Al-Pb dispersions under microgravity exhibited a rate constant with an intermediate value between theoretical predictions for pure diffusional Ostwald ripening (K_{LSW}) and pure Marangoni-driven coagulation (K_{coag}), consistent with the superposition $K_{\mathrm{total}} = K_{\mathrm{LSW}} + K_{\mathrm{coag}}$. Thus, Equation (15) can be used to describe coarsening kinetics of our system, where the physical interpretation of K will depend on which mechanism dominates or how multiple mechanisms combine.

Figure 6 compares the evolution of the average SiO_2 inclusion diameter in the E550, E321, and E136 samples with theoretical predictions from two models: (i) the Ostwald ripening model (green curves) based on the classical LSW theory (Equation (13)) using the theoretical rate constant and (ii) the collision-driven growth model (pink curves) based on the generalized cubic law (Equation (15)) with an effective rate constant K fitted to the experimental data. An initial particle radius of $r_0 = 0.1$ μm was adopted consistently across all experiments to represent the submicron SiO_2 nuclei formed immediately after deoxidation, before measurable coarsening begins. This choice is consistent with reported initial particle size in the study by Ohta et al. [14] and with the rapid diffusion-controlled growth predicted to occur within ~1 s (Figure 5), during which particles can already reach sizes comparable to the smallest experimentally measured diameters. After this brief diffusional growth stage, the growth mechanism transitions into Ostwald ripening or collision-driven coalescence.

Across all experiments, the collision-driven growth model predicts faster growth than the Ostwald coarsening model, reflecting the higher rate of collision-induced coalescence compared to Ostwald-controlled coarsening, except for E136. The experimental data in E136 indicates that both mechanisms (collision and Ostwald controlled) can act simultaneously, with their relative contributions determined primarily by the initial oxygen content.

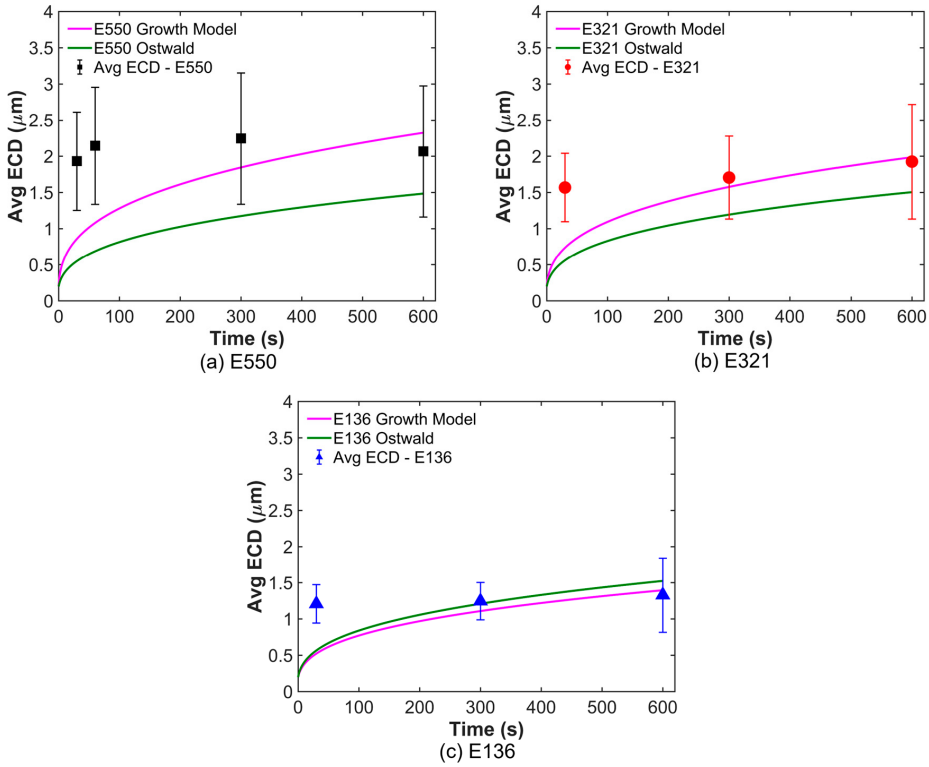

Figure 6. Comparison of average SiO_2 inclusion diameters in E550, E321, and E136 samples. Green curves: predictions from the Ostwald ripening model (Equation (13)) using the theoretical $K = \alpha_{LSW}\, k_d$. Pink curves: predictions from the collision-driven growth model (Equation (15)) with the effective rate constant K fitted to the experimental data. This figure illustrates that collision-driven coarsening dominates in oxygen-rich melts (E550, E321), whereas Ostwald-controlled diffusion governs coarsening in low-oxygen melts (E136).

Table 3 lists the fitted coarsening rate constants (K), extracted from the collision-growth model represented by the pink curves in Figure 6 for the three deoxidation experiments. The fitted K values decrease systematically from E550 to E136, indicating a reduction in collision frequency and coalescence efficiency as inclusion population and melt oxygen potential decline. This trend indicates a shift from a collision-dominated regime in oxygen-rich melts to a diffusion-controlled Ostwald regime in low-oxygen systems. The highest K value for E550 corresponds to rapid coalescence among closely spaced inclusions, whereas E321 exhibits moderate kinetics. In contrast, the lowest K value for E136 falls within the range characteristic of Ostwald ripening in molten steel, indicating that coarsening is increasingly governed by diffusion rather than particle collisions. The theoretical K value ($6.62 \times 10^{-4}\ \mu m^3/s$), calculated using Equation (13) (where $K = \alpha_{LSW}\, k_d$), also lies very close to the fitted constant, reinforcing that the growth mechanism in E136 has shifted from collision-driven coalescence to diffusion-controlled Ostwald ripening.

Table 3. Fitted coarsening rate constants K from the collision growth model (Equation (15)) for different deoxidation experiments.

Experiment	K ($\mu m^3/s$)
E550	2.61×10^{-3}
E321	1.63×10^{-3}
E136	5.64×10^{-4}

4.2. Collision Kinetics

To identify the dominant mechanisms governing the collision and subsequent growth of SiO_2 inclusions, different interaction pathways were evaluated, including Stokes-driven motion, Brownian motion, and Laminar shear-induced collisions, as proposed in earlier studies by Lei and He et al. [55] and Söder et al. [56]. The rate of change of the volumetric number density of inclusions within a given size group can be described by the population balance equation (PBE) formulated by Smoluchowski [42]. The governing equation expresses the rate of inclusion number density change in group k as the result of both inclusion coalescence (gain) and depletion (loss) processes:

$$\frac{dN_{v,k}}{dt} = \frac{1}{2}\sum_{i=1,\, i+j=k}^{k} \beta_{ij}^{C} N_{v,i} N_{v,j} - \sum_{i=1}^{k} \beta_{ik}^{C} N_{v,i} N_{v,k} \tag{16}$$

where $N_{v,i}$ and $N_{v,j}$ are the volumetric number densities of inclusions in groups i and j, respectively, and β_{ij}^{C} is the total collision frequency function that determines the rate of interaction between inclusions. The detailed expression used to calculate β_{ij}^{C} are given in Equations (17)–(19) [14,18,57].

$$\beta_{ij}^{S} = 2\pi(\rho_{steel} - \rho_p)\left(\frac{g}{9\mu}\right)(r_i + r_j)^3 |r_i - r_j| \tag{17}$$

$$\beta_{ij}^{B} = \frac{2\,k_B\,T}{3\,\mu}(r_i + r_j)\left(\frac{1}{r_i} + \frac{1}{r_j}\right) \tag{18}$$

$$\beta_{ij}^{LM} = \frac{4}{3}\frac{du}{dx}(r_i + r_j)^3 \tag{19}$$

The relative significance of Stokes motion, Brownian motion, and Laminar shear can be assessed by comparing their collision frequencies. Figure 7 shows the variation of the collision frequency function, β, for inclusion pairs with diameters d_i = 0.5, 1, 5, and 10 μm, while d_j varies from 0 to 20 μm. Here, β^S, β^B, and β^L denote the collision frequencies associated with Stokes (buoyancy-driven) motion, Brownian motion, and Laminar shear, respectively. These dimensions represent the size range of SiO_2 inclusions observed experimentally (Figure 2). The viscosity of steel was taken as 5.07×10^{-3} kg/(m·s) at 1873 K, with steel and SiO_2 inclusion densities of 7000 and 2650 kg/m^3, respectively.

For inclusions in the 1–5 μm range observed in the present experiments, Stokes collision emerges as the dominant growth mechanism. As shown in Figure 7, the Stokes collision frequency, β^S, exceeds the Brownian collision frequency, β^B, when $d_i \geq 1$ μm and $d_j \geq 2$ μm. This increase arises from the differential settling velocities between inclusions of unequal sizes due to buoyancy-driven motion, while inclusions of similar diameters ($d_i \approx d_j$) exhibit minimal relative velocity and thus show a characteristic minimum in β^S near $d_i = d_j$. In contrast, β^B remains relatively constant at around 10^{-17} to 10^{-16} m^3/s across all d_i values, with only slightly higher values at smaller diameters, confirming that Brownian motion plays a minor role for the particle size distribution observed experimentally.

Furthermore, the mean displacement of a particle due to Brownian motion after a time t is expressed as

$$\lambda = \sqrt{2Dt} = \sqrt{\frac{2k_B T t}{3\pi\mu d}} \tag{20}$$

where λ represents the average distance that a particle travels from its original position as a result of random collisions. The mean displacement of SiO_2 particles was estimated for particle diameters of 0.1, 1, and 2 μm at 1873 K for t = 1 s, assuming a liquid steel viscosity of 5.07×10^{-3} Pa·s [41], as calculated using Equation (5). These values, summarized in

Table 4, were used to assess the extent to which Brownian motion could contribute to inclusion motion and collision during the deoxidation process.

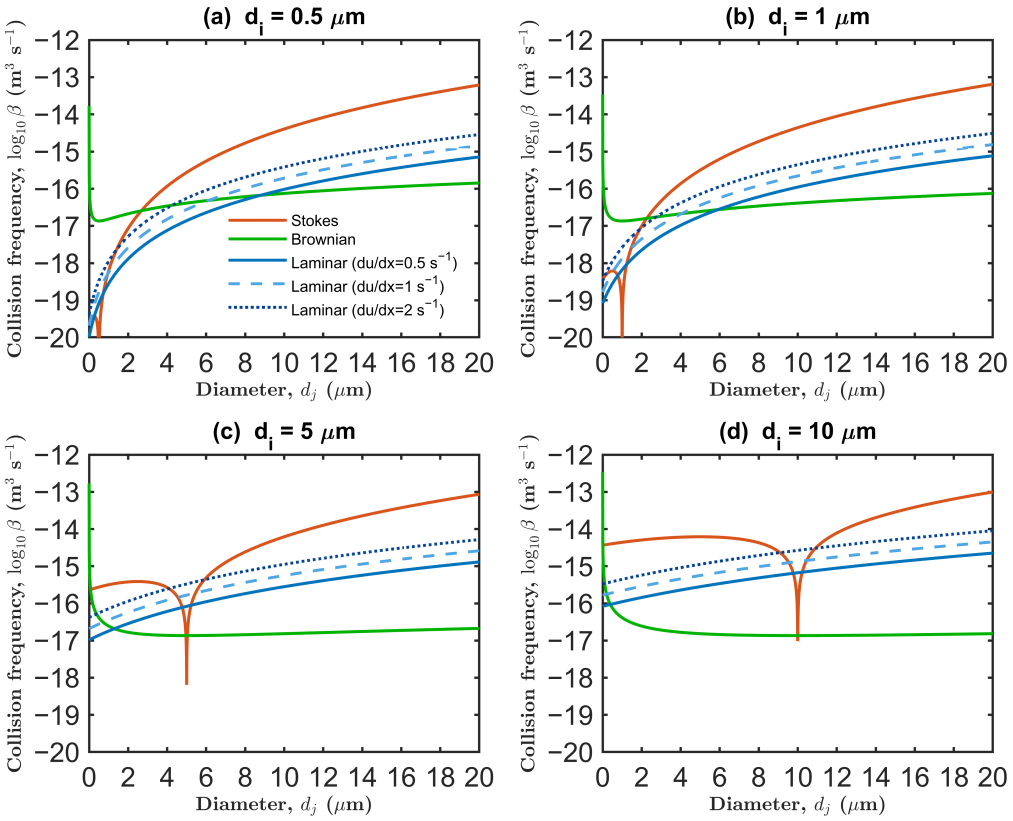

Figure 7. Comparison of collision frequency functions for Stokes, Brownian and Laminar mechanisms for SiO_2 inclusions with fixed primary diameters of (**a**) 0.5 µm, (**b**) 1 µm, (**c**) 5 µm, and (**d**) 10 µm, as a function of varying partner diameter (d_j).

Table 4. Calculated Brownian diffusivity and mean displacement of SiO_2 particles in liquid steel at 1873 K for $t = 1$ s.

Particle Diameter, d (µm)	Diffusivity, D (m^2/s)	Mean Displacement, λ (µm)
0.1	5.4×10^{-12}	3.3
1.0	5.4×10^{-13}	1.0
2.0	2.7×10^{-13}	0.7

The results show that Brownian motion weakens markedly with increasing particle size. For a 0.1 µm inclusion, the calculated mean displacement after 1 s is about 3–4 µm, suggesting that ultrafine nuclei can move several micrometers per second due to random atomic impacts. However, for 2 µm inclusions, the displacement decreases to approximately 0.7 µm, which is small relative to the typical inter-particle separation distances in the melt. Thus, it can be said that Brownian motion can promote collisions only during the very early stages of deoxidation when submicron SiO_2 nuclei are abundant. Theoretical calculations suggest these particles agglomerate quickly into the observable >1 µm range within the first few seconds of deoxidation.

In addition, the Laminar shear collision frequency, β^{L}, was evaluated to account for velocity gradients within the melt. For the present vertical tube furnace operating under stagnant conditions without forced stirring, a conservative shear rate of $du/dx = 0.5\ s^{-1}$ was assumed to account for minimal natural convection driven by thermal gradients, whereas higher gradients up to $du/dx = 2\ s^{-1}$ are typically reported for induction furnaces where melt convection is more pronounced [58]. As shown in Figure 7, the Laminar shear contribution at $du/dx = 0.5\ s^{-1}$ lies below both the Stokes and Brownian collision frequencies for the majority of the particle size range examined. Even at higher shear rates (1–2 s^{-1}), β^{L} approaches β^{S} only for larger inclusions ($d_i \geq 5$ μm), indicating that the effect of shear-induced collisions remains secondary under the current experimental conditions. Therefore, Stokes collision is identified as the primary mechanism responsible for inclusion growth throughout most of the holding period, with minor contributions from Brownian motion (dominant only for smaller inclusions size). However, the effectiveness of Stokes-driven collisions depends strongly on the particle size distribution (PSD). In E136, the PSD is dominated by submicron and small inclusions (Figure 4), which reduces the frequency of differential settling and limits the overall contribution of Stokes-driven collisions in that melt. This reduced contribution is thus a consequence of the PSD shape in E136, rather than a contradiction of the collision mechanism itself. In contrast, the higher fraction of larger inclusions in E550 and E321 (Figure 4) promotes frequent differential settling, causing Stokes-driven collisions to dominate their growth behavior.

4.3. Removal Kinetics

In the preceding sections, inclusion growth and coarsening were examined in terms of diffusion-controlled Ostwald ripening and collision-driven mechanisms. In practice, however, the evolution of the inclusion population is also strongly influenced by removal through flotation. This section therefore focuses specifically on the kinetics of inclusion removal from the melt and its coupling with the already-established growth processes, with emphasis on how flotation modifies the temporal evolution of inclusion number density and volume fraction. Such removal effects are known to play a key role in shaping the final particle size distribution, often resulting in lognormal shaped particle distributions [23,47].

To account for both collision-driven growth and flotation-driven removal, one can model the temporal variation of inclusion number density (N_V) during deoxidation as

$$\frac{dN_V}{dt} = -\frac{1}{2}K_{coll}N_V^2 - K_{rem}N_V \tag{21}$$

Here, K_{coll} represents the collision coefficient ($mm^3/(\#\cdot s)$) and K_{rem} is the size-independent removal coefficient (s^{-1}). The first term captures the quadratic decay in N_V due to inclusion–inclusion coalescence, while the second term accounts for the first-order removal by flotation to the melt surface. Although flotation is intrinsically size-dependent, K_{rem} is treated here as an effective, size-averaged removal coefficient representing the net behavior of the inclusion population in this first-order approximation.

Figure 8 compares the experimentally measured and fitted N_V values for E550 and E321. Both datasets show a steady decline in inclusion number density with time, consistent with simultaneous coalescence and removal. The fitted kinetic parameters (K_{coll} and K_{rem}) for both experiments, listed in Table 5, provide insight into the relative contributions of collision and removal processes.

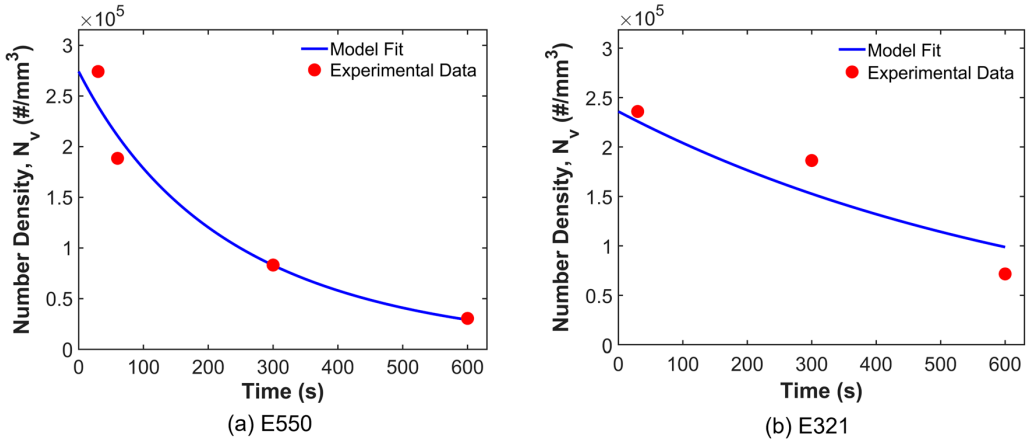

Figure 8. Temporal variation of inclusion number density (N_V) for E550 and E321. Solid curves represent model predictions from the coupled population-balance equation

In E550, N_V decreases sharply, from 2.7×10^5 to 3.1×10^4 (#/mm^3), indicating rapid loss of inclusions. The fitted kinetic parameters $K_{coll} = 9.5 \times 10^{-9}$ (mm^3/(#·s)) and $K_{rem} = 3.24 \times 10^{-3}$ s^{-1} (see Table 5), show that both coalescence and removal are highly active under the oxygen-rich conditions of this experiment. The large K_{coll} value, when compared against the values obtained for the other experiments, reflects the high collision frequency associated with the initially dense inclusion population, while the pronounced removal rate (K_{rem}) indicates efficient flotation of larger inclusions once they form. This coupling between coalescence and flotation creates a self-reinforcing mechanism: rapid collision-driven growth produces larger inclusions that float more readily, thereby accelerating the overall removal kinetics beyond what either process would achieve independently.

In contrast, E321 exhibits a more gradual decrease in N_V (from 2.4×10^5 to 7.2×10^4 (#/mm^3)), consistent with a substantially lower collision coefficient, $K_{coll} = 2.3 \times 10^{-14}$ (mm^3/(#·s)). This small value, compared to E550, suggests that collision-driven coalescence plays a minor role in E321. This five-orders-of-magnitude reduction in K_{coll} arises mainly from the lower inclusion density and smaller particle sizes in E321, which reduce collision probability. Instead, the dominant term governing the decay in N_V is the first-order removal term, characterized by $K_{rem} = 1.45 \times 10^{-3}$ s^{-1}. The reduced contribution of coalescence is consistent with the smaller average inclusion size and lower population density observed in E321 (see Figure 2).

Table 5. Estimated kinetic parameters K_{coll} and K_{rem} for inclusion population evolution in E550 and E321 experiments.

Experiment	K_{coll} (mm^3/#·s)	K_{rem} (s^{-1})
E550	9.5×10^{-9}	3.24×10^{-3}
E321	2.3×10^{-14}	1.45×10^{-3}

Overall, the population shifts from collision-enhanced growth with strong subsequent removal in E550 to a regime in E321 where both coalescence and removal remain active but with comparatively weaker collision contributions. The observed decline in N_V closely mirrors the reduction in volume fraction (f_v), confirming that both coalescence and flotation jointly govern inclusion population dynamics. To elucidate this further, one can model the temporal evolution of the inclusion volume fraction as

$$f_v(t) = f_v(0)\, \exp\left(-\alpha\, r^2(t)\, t\right), \tag{22}$$

where $f_v(0)$ is the initial inclusion volume fraction and α is an empirical removal parameter representing the rate at which inclusions are consumed or eliminated from the melt. In this formulation, the decrease in f_v is governed primarily by the size of the inclusions rather than the number present. The $r^2(t)$ term in Equation (22) originates from Stokes flotation [9,18], where the rising velocity of a particle in a viscous fluid increases with the square of its radius. As inclusions grow, their buoyancy-driven flotation becomes more efficient, leading to a faster depletion of the dispersed phase. Because f_v represents the total inclusion volume per unit volume of steel, the exponential decay captures how removal accelerates as particles become larger and float out more readily, independent of the population count.

Table 6 reports the fitted removal parameter (α) for E550 and E321. The larger α value in E550 indicates a faster depletion of the dispersed phase, consistent with its larger average inclusion size, which enhances flotation once coalescence has produced a population of large particles. Together, the higher K_{rem} and α values (Tables 5 and 6) confirm that, although E550 is collision-dominated in terms of coarsening kinetics (as indicated by its large K_{coll}), removal becomes highly efficient once large inclusions form.

Table 6. Estimated removal parameter α for E550 and E321 experiments.

Experiment	α (1/(μm^2·s))
E550	3.5×10^{-3}
E321	1.6×10^{-3}

It needs to be noted that the kinetic parameters K_{coll} and α were not extracted for E136 because the assumptions underlying the simplified collision–removal model (Equation (21)) no longer hold. This is because the inclusion population in this melt is dominated by small particles, leading to possible contributions from both Brownian collisions and Ostwald ripening (see Figure 6), while the removal rate is slow; as a result, there is no single dominant collision mechanism, and the assumption of size-independent removal is violated. Further work is necessary to quantify the relationship between inclusion volume fraction and size-dependent removal in such systems.

4.4. Population Density Function

The calculated PDF plots (using Equation (12)) of silica inclusions over each inclusion size are presented in Figure 9 on a logarithmic scale for all three experiments: E550, E321, and E136. Across all cases, a linear decrease with some scatter, irrespective of oxygen contents, was observed, indicating a fractal distribution. A fractal distribution observed in the PDF indicates that inclusion growth is governed by a steady-state balance between removal and coalescence after solute–inclusion equilibrium is reached [45–49].

Since the number of data points below 1 μm is not available, it is not sufficient to conclusively establish a lognormal distribution. Instead, the slope of ln(PDF) versus log(size) is used to describe how rapidly the particle population density decreases with increasing size. The calculated slopes of −7.5 for E550, −10.3 for E321, and −13.1 for E136 reveal distinct coarsening behaviors. The least negative slope in E550 indicates a broader size distribution with particle growth, consistent with Stokes collision–dominated growth. E321 shows an intermediate slope, also reflecting Stokes-driven growth, while the steepest slope in E136 suggests a finer inclusion population where Brownian motion governs the collision mechanism.

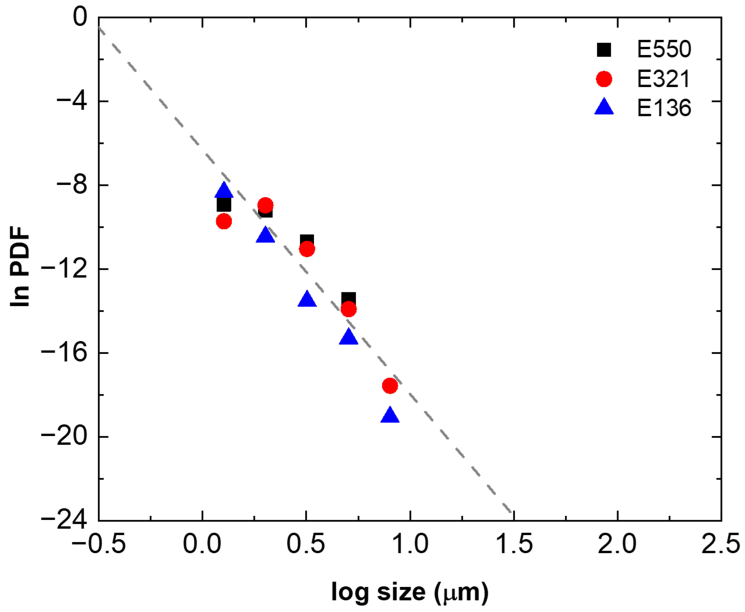

Figure 9. PDF plots of silica inclusions as a function of inclusion size across three different experiments.

These findings are consistent with the results of Kim et al. [23], who reported that preferential Si addition in Fe–1.5Al–xSi (x = 0.5–3.0 wt.%) steels led to the formation of spherical SiO_2 inclusions with power-law PDF distributions, confirming collision-driven growth. In contrast, subsequent Al addition transformed the inclusions into Al_2O_3-rich and $MgAl_2O_4$ spinel phases, resulting in lognormal PDF distributions characteristic of diffusion-controlled growth. In the present study, the power-law distribution observed in the PDF across all the three experiments (Figure 9) suggests that inclusion growth is primarily governed by a collision-driven mechanism, with each SiO_2 inclusion originating from the FeSi deoxidation reaction. Even though, some of the inclusions are removed by flotation as discussed in Section 4.3, the average inclusion size gradually increases with time following the addition of FeSi, as shown in Figure 2.

Figure 10 presents the normalized particle size distributions for silica inclusions in E550, E321, and E136 at 600 s, plotted as a function of the normalized radius $\rho = r/\bar{r}_{geo}$, where $\bar{r}_{geo}$ is the geometric mean radius. The solid black curve corresponds to the theoretical Lifshitz–Slyozov–Wagner (LSW) distribution for diffusion-controlled Ostwald ripening [35]. The comparison is made specifically at 600 s because, by this stage, the inclusion volume fraction has decreased substantially (see Figure 3), consistent with the LSW expectation that f_V becomes negligible as coarsening progresses. This shows that as larger inclusions are removed, the system tends to approach the dilute regime required for Ostwald ripening.

4.5. Growth Mechanisms

In E136, the distribution in Figure 10 shows a good agreement with LSW theory, with peak occurring near at $\rho \approx 1.0$, very close to the theoretical LSW peak at $\rho = 1.12$. The experimental curves display a sharp cutoff near $\rho = 1.5$, consistent with the LSW prediction of a maximum particle size of 1.5 times the mean radius. The tendency toward Ostwald ripening is evident from the relatively low and nearly constant volume fraction of inclusions, together with the slow rate of its decrease over time, indicating diffusion-controlled coarsening. The measured inclusion volume fractions lie between 8.1×10^{-4} and 1.4×10^{-4} for E136. These values are comparable to those reported in the literature where Ostwald ripening was identified as the predominant coarsening mechanism. Ohta and Suito [14] observed that when the particle volume fraction was approximately 4×10^{-4} in Fe–10 mass%Ni alloys, particle growth occurred predominantly by Ostwald ripening in

the absence of convective motion. Similarly, Suzuki et al. [15] also concluded that inclusion growth during solidification of Si/Mn-deoxidized stainless steel followed Ostwald ripening kinetics at comparable low particle volume fractions (8.1×10^{-4}). Furthermore, this interpretation is supported by the evolution of the dimensionless coarsening coefficient, α_{LSW}, which is defined in Equation (13). As shown in Figure 11, α_{LSW} exhibits its highest value at 30 s ($\alpha_{LSW} = 5.91$) but decreases sharply with holding time, reaching 0.63 at 300 s and 0.46 at 600 s. These latter values lie very close to the theoretical LSW limit of $\alpha_{LSW} = 0.444$ for diffusion-controlled Ostwald ripening [35]. However, it can be surmised that Brownian collision effects are also present. As shown in Figure 4, most inclusions in E136 lie within the 1–2 μm size range, where Brownian collisions play an important role and, thus, can contribute to growth, as discussed in Section 4.2.

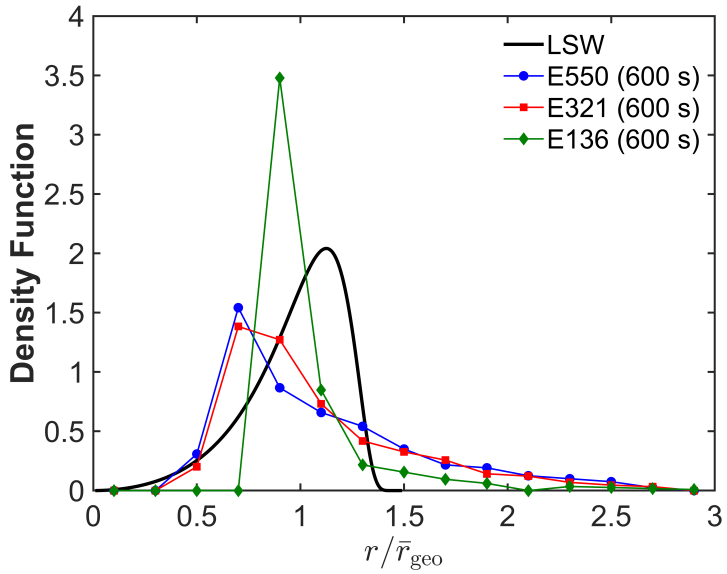

Figure 10. Variation of density function at 600 s at 1873 K in E550, E321 and E136.

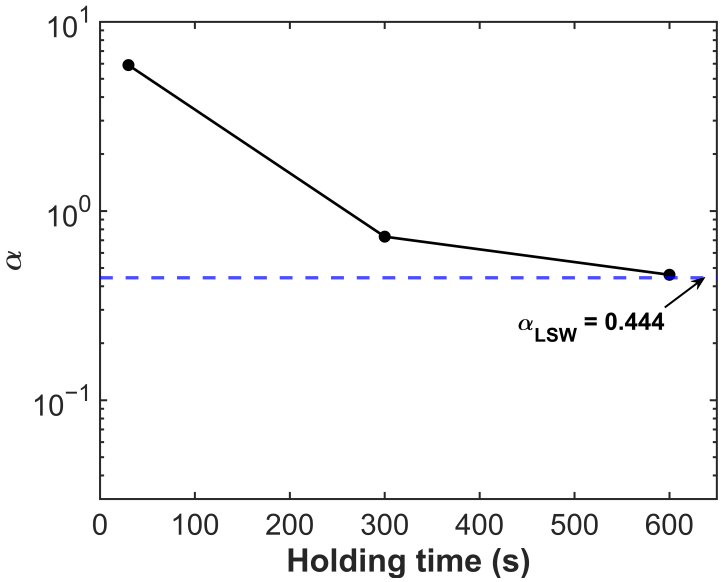

Figure 11. Variation of coarsening coefficient (α_{LSW}) with holding time in E136.

In contrast to E136, the E321 and E550 samples exhibit progressively stronger Stokes-driven collision mechanisms. For E321, the moderate oxygen content produces an intermediate regime where size-dependent ascending velocity differences begin to enhance collision-driven growth, as evidenced by the higher volume fraction and the increasing

prevalence of 3–4 μm inclusions (Figure 4). In E550, the high initial oxygen content generates a dense inclusion population that maximizes Stokes collision frequency, with the resulting polydispersity further enhancing coalescence probability.

As shown in Figure 2, the average ECD for E550 samples increases steadily before exhibiting a slight decline at 600 s, whereas E321 and E136 samples display consistent growth throughout the observation period. This behavior reflects the rapid formation of large inclusions (3–5 μm) in E550, which are subsequently removed by flotation, ultimately shifting the remaining population toward finer sizes (Figure 10).

This characteristic is consistent with the numerical predictions of Zhang and Lee [57], who developed a general nucleation–growth model integrating homogeneous nucleation with multiple growth mechanisms for alumina inclusions in Al-killed steel at 1873 K. Their simulations revealed that the mean particle size initially increases, reaches a maximum, and subsequently decreases as removal of large inclusions begins to dominate, indicating a balance between growth and removal processes. Their prediction is consistent with the experimental behaviour observed for the E550 samples in the present study, where we observed the highest removal rate (see Figure 3), which leads to a decrease in the mean size at longer holding times (see Figure 2). This agreement reinforces the conclusion that Stokes collisions and subsequent flotation become dominant once a sufficient population of large inclusions has formed.

5. Conclusions

The experimental results in our study show clearly that SiO_2 inclusions collide and coalesce in liquid steel, leading to their subsequent growth and removal. The growth of inclusions under such conditions follows the $t^{1/3}$ scaling law. Furthermore, it is seen that initial oxygen plays a role in deciding the particle size distribution studied in this work that determines the active growth mechanisms operating on the inclusions. Specifically, under our laboratory conditions, it is seen that lower oxygen leads to a slower inclusion growth driven by Brownian collisions and Ostwald ripening mechanisms, owing to the presence of small size inclusions (1–2 μm). On the other hand, higher oxygen in steel leads to rapid growth of inclusions to larger sizes by Stokes collisions, which get removed fast by flotation, leaving behind inclusions ranging from 1 to 5 μm.

The above findings are otherwise difficult to obtain in industrial settings, as growth is primarily influenced by inertial forces and turbulence caused by Ar stirring. However, in any case, these results should help steelmakers in optimizing alloy addition timing sequences to produce cleaner steel under different levels of oxygen. The study also shows the usefulness of holistic analyses of volume fraction and size distribution dynamics to unravel the underlying growth and removal mechanisms of inclusions in liquid steel.

Future research will extend this framework to investigate the compositional evolution of SiO_2 inclusions into Mn-silicate or complex oxide phases during secondary metallurgy, while also examining the influence of ferrosilicon purity and residual Al content on inclusion evolution. Higher-resolution SEM analysis will be employed to capture sub-micron inclusions and better characterize Brownian collision kinetics. Additionally, future work will focus on inclusion capture at crucible walls and melt surfaces, as well as the effects of dynamic process conditions (e.g., controlled stirring) on inclusion growth and removal kinetics relevant to industrial ladle metallurgy.

Author Contributions: Conceptualization, S.K. and N.D.; methodology, S.K., A.P., M.N., A.B.P. and N.D.; software, S.K.; validation, S.K., A.P. and M.N.; formal analysis, S.K. and A.P.; investigation, S.K., A.P., M.N., A.B.P. and N.D.; resources, A.B.P. and N.D.; data curation, S.K., A.P., M.N., A.B.P. and N.D.; writing—original draft preparation, S.K.; writing—review and editing, A.P., M.N., A.B.P. and N.D.; visualization, S.K.; supervision, A.B.P. and N.D.; project administration, A.B.P.; funding acquisition, A.B.P. and N.D. All authors have read and agreed to the published version of the manuscript.

Funding: This research was funded by the Natural Sciences and Engineering Research Council of Canada (NSERC).

Data Availability Statement: The original contributions presented in this study are included in the article. Further inquiries can be directed to the corresponding author.

Acknowledgments: Appreciation is also extended to the Canadian Centre for Electron Microscopy (CCEM) at McMaster University for providing facilities and support for materials characterization.

Conflicts of Interest: The authors declare no conflicts of interest.

Appendix A. Calculation of Interfacial Energy Between Oxide and Molten Steel

The interfacial energy between the oxide and molten steel, γ_{PL} (J/m^2), is determined as

$$\gamma_{PL} = \gamma_P - \gamma_L \cdot \cos\theta_{PL} \tag{A1}$$

where the contact angle (θ) is 115° [59]. For the surface tension of the particle, γ_P, a value of 0.4 J/m^2 [60] is used based on the assumption of the particle being silica while the surface tension of the liquid metal, γ_L, term is calculated using a correlation derived from the Gibbs–Langmuir adsorption isotherm. This approach, as described by Chung and Cramb [61], builds upon the methods developed by Belton [62] and Sahoo et al. [63]:

$$\gamma_L = 1913 + 0.43[1823 - T] + 67.75\,[\text{wt.\% C}] - 0.10T\ln(1 + K_s a_s) - 0.153T\ln(1 + K_o a_o) \tag{A2}$$

where the adsorption coefficients of oxygen K_O and sulphur K_S on liquid iron alloys are determined using the relationships below [61]:

$$\log K_O = 11370/T - 4.09 \tag{A3}$$

$$\log K_S = 10013/T - 2.87 \tag{A4}$$

and the activities of oxygen and sulfur are calculated via Henry's law using the activity coefficients expressed as

$$\log f_i = e_i^O[\%O] + e_i^S[\%S] + e_i^C[\%C] \tag{A5}$$

where f_i is the activity coefficient for species i (oxygen and sulfur); e_i^O, e_i^S and e_i^C represent the first-order interaction parameters found in [64].

References

1. Chen, C.; Jiang, Z.; Li, Y.; Zheng, L.; Huang, X.; Yang, G.; Sun, M.; Chen, K.; Yang, H.; Hu, H.; et al. State of the art in the control of inclusions in tire cord steels and saw wire steels–a review. *Steel Res. Int.* **2019**, *90*, 1800547. [CrossRef]
2. Kang, Y.B.; Lee, H.G. Inclusions chemistry for Mn/Si deoxidized steels: Thermodynamic predictions and experimental confirmations. *ISIJ Int.* **2004**, *44*, 1006–1015. [CrossRef]
3. Kaushik, P.; Lehmann, J.; Nadif, M. State of the art in control of inclusions, their characterization, and future requirements. *Metall. Mater. Trans. B* **2012**, *43*, 710–725. [CrossRef]
4. Luiz, A.; Costa e Silva, V. Non-metallic inclusions in steels—Origin and control. *J. Mater. Res. Technol.* **2018**, *7*, 283–299.
5. Ghosh, A.; Chatterjee, A. *Iron Making and Steelmaking: Theory and Practice*; PHI Learning Pvt. Ltd.: Delhi, India, 2008.

6. Kemeny, F.L. Tundish nozzle clogging-measurement and prevention. In *Alex McLean Symposium: Process Fundamentals, Liquid Metal Processing for Cleanliness, Novel and Conventional Casting, and Novel Process Technologies*; The Iron and Steel Society: Warrendale, PA, USA, 1998; pp. 103–110.
7. Dressel, G.L. Silicon Killed Steel Nozzle Clogging. Available online: https://www.yumpu.com/en/document/view/12111153/ (accessed on 15 April 2025).
8. Turkdogan, E. Nucleation, growth, and flotation of oxide inclusions in liquid steel. *J. Iron Steel Inst.* **1966**, *204*, 914–919.
9. Miyashita, Y. *Nippon Kokan Technical Report*; Nippon Kokan K.K.: Tokyo, Japan, 1965; p. 29.
10. Taniguchi, S.; Kikuchi, A. Mechanisms of collision and coagulation between fine particles in fluid. *Tetsu-to-Hagane* **1992**, *78*, 527–535. [CrossRef] [PubMed]
11. Piva, S.P.; Pistorius, P.C. Aluminum-free steelmaking: Desulfurization and nonmetallic inclusion evolution of Si-killed steel in contact with CaO-SiO2-CaF2-MgO slag. *Processes* **2021**, *9*, 1258. [CrossRef]
12. Zhang, L. State of the Art in the Control of Inclusions in Tire Cord Steels-a Review. *Steel Res. Int.* **2006**, *77*, 158–169. [CrossRef]
13. Zhang, L.; Guo, C.; Yang, W.; Ren, Y.; Ling, H. Deformability of oxide inclusions in tire cord steels. *Metall. Mater. Trans. B* **2018**, *49*, 803–811. [CrossRef]
14. Ohta, H.; Suito, H. Effects of dissolved oxygen and size distribution on particle coarsening of deoxidation product. *ISIJ Int.* **2006**, *46*, 42–49. [CrossRef]
15. Suzuki, M.; Yamaguchi, R.; Murakami, K.; Nakada, M. Inclusion particle growth during solidification of stainless steel. *ISIJ Int.* **2001**, *41*, 247–256. [CrossRef]
16. Kluken, A.; Grong, Ø. Mechanisms of inclusion formation in Al- Ti- Si- Mn deoxidized steel weld metals. *Metall. Trans. A* **1989**, *20*, 1335–1349. [CrossRef]
17. Wang, L.; Li, J.; Yang, S.; Chen, C.; Jin, H.; Li, X. Coarsening behavior of particles in Fe-O-Al-Ca melts. *Sci. Rep.* **2019**, *9*, 3670. [CrossRef]
18. Lindberg, U.; Torsell, K. A Collision Model for the Growth and Separation of Deoxidation Products. *Trans. Metall. Soc. AIME* **1968**, *242*, 94–102.
19. Engh, T.; Lindskog, N. A fluid mechanical model of inclusion removal. *Scand. J. Metall.* **1975**, *4*, 49–58.
20. Saffman, P.; Turner, J. On the collision of drops in turbulent clouds. *J. Fluid Mech.* **1956**, *1*, 16–30. [CrossRef]
21. Liu, Z.; Song, G.; Deng, Z.; Zhu, M. Evolution of inclusions in Si-Mn-killed steel during ladle furnace (LF) refining process. *Metall. Mater. Trans. B* **2021**, *52*, 1243–1254. [CrossRef]
22. Miao, K.; Nabeel, M.; Dogan, N. Coarsening Mechanisms of CaS Inclusions in Ca-Treated Steels. *Metals* **2022**, *12*, 707. [CrossRef]
23. Kim, T.S.; Park, G.H.; Kim, D.W.; Park, J.H. Evolution Mechanism of Nonmetallic Inclusions in Fe-1.5 Al-xSi (x= 0.5–3.0 wt%) Alloyed Steels. *Steel Res. Int.* **2024**, *96*, 2400491. [CrossRef]
24. Ferreira, M.E.; Pistorius, P.C.; Fruehan, R.J. Liquid inclusion collision and agglomeration in calcium-treated aluminum-killed steel. *Front. Mater.* **2021**, *8*, 736807. [CrossRef]
25. Turpin, M.; Elliott, J. Nucleation of oxide inclusions in iron melts. *J. Iron Steel Inst.* **1966**, *204*, 217–225.
26. Rocabois, P.; Lehmann, J.; Gaye, H.; Wintz, M. Kinetics of precipitation of non-metallic inclusions during solidification of steel. *J. Cryst. Growth* **1999**, *198*, 838–843. [CrossRef]
27. Zener, C. Theory of growth of spherical precipitates from solid solution. *J. Appl. Phys.* **1949**, *20*, 950–953. [CrossRef]
28. Hong, T.; Debroy, T.; Babu, S.; David, S. Modeling of inclusion growth and dissolution in the weld pool. *Metall. Mater. Trans. B* **2000**, *31*, 161–169. [CrossRef]
29. Zhang, L.; Thomas, B.G. State of the art in evaluation and control of steel cleanliness. *ISIJ Int.* **2003**, *43*, 271–291. [CrossRef]
30. Miki, Y.; Thomas, B.G. Modeling of inclusion removal in a tundish. *Metall. Mater. Trans. B* **1999**, *30*, 639–654. [CrossRef]
31. Ohta, H.; Suito, H. Characteristics of particle size distribution of deoxidation products with Mg, Zr, Al, Ca, Si/Mn and Mg/Al in Fe–10mass% Ni alloy. *ISIJ Int.* **2006**, *46*, 14–21. [CrossRef]
32. Girifalco, L.; Behrendt, D. Mathematics of diffusion-controlled precipitation in the presence of homogeneously distributed sources and sinks. *Phys. Rev.* **1961**, *124*, 420. [CrossRef]
33. Gaskell, D.R. *Introduction to the Thermodynamics of Materials*; Taylor and Francis: New York, NY, USA; London, UK, 2008.
34. Wert, C.; Zener, C. Interference of growing spherical precipitate particles. *J. Appl. Phys.* **1950**, *21*, 5–8. [CrossRef]
35. Lifshitz, I.M.; Slyozov, V.V. The kinetics of precipitation from supersaturated solid solutions. *J. Phys. Chem. Solids* **1961**, *19*, 35–50. [CrossRef]
36. Wagner, C. Theory of the aging of precipitates by dissolution-reprecipitation (Ostwald ripening). *Z. Elektrochem.* **1961**, *65*, 581–591.
37. Baldan, A. Review Progress in Ostwald ripening theories and their applications to nickel-base superalloys Part I: Ostwald ripening theories. *J. Mater. Sci.* **2002**, *37*, 2171–2202. [CrossRef]
38. Yao, J.H.; Elder, K.; Guo, H.; Grant, M. Theory and simulation of Ostwald ripening. *Phys. Rev. B* **1993**, *47*, 14110. [CrossRef]
39. Voorhees, P.W. The theory of Ostwald ripening. *J. Stat. Phys.* **1985**, *38*, 231–252. [CrossRef]

40. Einstein, A. *Investigations on the Theory of the Brownian Movement*; Courier Corporation: Chelmsford, MA, USA, 1956.
41. Brooks, R.F.; Day, A.P.; Andon, R.J.; Chapman, L.A.; Mills, K.C.; Quested, P.N. Measurement of viscosities of metals and alloys with an oscillating viscometer. *High Temp. High Press.* **2001**, *33*, 73–82. [CrossRef]
42. Smoluchowski, M. Mathematical theory of the kinetics of the coagulation of colloidal solutions. *Z. Phys. Chem.* **1917**, *92*, 129–168.
43. Podder, A. Modelling Transient Inclusion Behaviour During Refining of Si-Mn Killed Steel. Ph.D. Thesis, McMaster Univeristy, Hamilton, ON, Canada, 2023.
44. Fullman, R. Measurement of particle sizes in opaque bodies. *Jom* **1953**, *5*, 447–452. [CrossRef]
45. Van Ende, M.A.; Guo, M.; Zinngrebe, E.; Dekkers, R.; Proost, J.; Blanpain, B.; Wollants, P. Morphology and growth of alumina inclusions in Fe–Al alloys at low oxygen partial pressure. *Ironmak. Steelmak.* **2009**, *36*, 201–208. [CrossRef]
46. Zinngrebe, E.; Van Hoek, C.; Visser, H.; Westendorp, A.; Jung, I.H. Inclusion population evolution in Ti-alloyed Al-killed steel during secondary steelmaking process. *ISIJ Int.* **2012**, *52*, 52–61. [CrossRef]
47. Van Ende, M.A.; Guo, M.; Zinngrebe, E.; Blanpain, B.; Jung, I.H. Evolution of non-metallic inclusions in secondary steelmaking: Learning from inclusion size distributions. *ISIJ Int.* **2013**, *53*, 1974–1982. [CrossRef]
48. Seo, M.D.; Cho, J.W.; Kim, K.C.; Kim, S.H. Evolution of non-metallic inclusions in ultra low carbon steel after aluminum deoxidization. *ISIJ Int.* **2014**, *54*, 475–481. [CrossRef]
49. Kim, T.S.; Lee, S.B.; Park, J.H. Effect of tundish flux on compositional changes in non-metallic inclusions in stainless steel melts. *ISIJ Int.* **2021**, *61*, 2998–3007. [CrossRef]
50. Kim, T.S.; Yang, J.; Park, J.H. Effect of physicochemical properties of slag on the removal rate of alumina inclusions in the ruhrstahl–heraeus (RH) refining conditions. *Metall. Mater. Trans. B* **2022**, *53*, 2523–2533. [CrossRef]
51. Park, J.S.; Park, J.H. Effect of physicochemical properties of slag and flux on the removal rate of oxide inclusion from molten steel. *Metall. Mater. Trans. B* **2016**, *47*, 3225–3230. [CrossRef]
52. Suzuki, K.; Mori, K. Diffusion of oxygen in molten iron. *Tetsu-to-Hagané* **1971**, *57*, 2219–2229. [CrossRef]
53. Wang, L.; Li, J.; Yang, S.; Chen, C.; Jin, H.; Li, X. Nucleation and ostwald growth of particles in Fe-O-Al-Ca melt. *Sci. Rep.* **2018**, *8*, 1135. [CrossRef] [PubMed]
54. Ratke, L. Coarsening of liquid Al-Pb dispersions under reduced gravity conditions. *Mater. Sci. Eng. A* **1995**, *203*, 399–407. [CrossRef]
55. Lei, H.; He, J. Nucleation and growth kinetics of MgO in molten steel. *J. Mater. Sci. Technol.* **2012**, *28*, 642–646. [CrossRef]
56. Söder, M.; Jönsson, P.; Jonsson, L. Inclusion Growth and Removal in Gas-Stirred Ladles. *Steel Res. Int.* **2004**, *75*, 128–138. [CrossRef]
57. Zhang, J.; Lee, H.G. Numerical modeling of nucleation and growth of inclusions in molten steel based on mean processing parameters. *ISIJ Int.* **2004**, *44*, 1629–1638. [CrossRef]
58. Piva, S.P.T. Non-Metallic Inclusion Changes in Si-Mn Killed Steels. Ph.D. Thesis, Carnegie Mellon University, Pittsburgh, PA, USA, 2018.
59. O'Malley, R.J. Inclusion evolution and removal in ladle refining. In Proceedings of the AISTech 2017 Conference and Exposition, Nashville, TN, USA, 8–11 May 2017.
60. Mu, W.; Dogan, N.; Coley, K.S. Agglomeration of non-metallic inclusions at the steel/Ar interface: Model application. *Metall. Mater. Trans. B* **2017**, *48*, 2092–2103. [CrossRef]
61. Chung, Y.; Cramb, A.W. Dynamic and equilibrium interfacial phenomena in liquid steel-slag systems. *Metall. Mater. Trans. B* **2000**, *31*, 957–971. [CrossRef]
62. Belton, G. Langmuir adsorption, the Gibbs adsorption isotherm, and interfacial kinetics in liquid metal systems. *Metall. Mater. Trans. B* **1976**, *7*, 35–42. [CrossRef]
63. Sahoo, P.; Debroy, T.; McNallan, M. Surface tension of binary metal—surface active solute systems under conditions relevant to welding metallurgy. *Metall. Trans. B* **1988**, *19*, 483–491. [CrossRef]
64. Sigworth, G.K.; Elliott, J.F. The thermodynamics of liquid dilute iron alloys. *Met. Sci.* **1974**, *8*, 298–310. [CrossRef]